Empty-bucket techniques for spill-quality improvement at the CERN Super Proton Synchrotron

Pablo A. Arrutia Sota,* Matthew A. Fraser, Gregoire Hagmann, Verena Kain, Giulia Papotti, Arthur Spierer, and Francesco M. Velotti
CERN, Geneva, Switzerland

Philip N. Burrows
John Adams Institute, University of Oxford, Oxford, United Kingdom

Roberto Piandani
CERN, Geneva, Switzerland and Instituto de Física, Universidad Autónoma de San Luis Potosí, 78240 San Luis Potosí, Mexico

(Received 4 December 2023; accepted 12 June 2024; published 9 July 2024)

Synchrotrons can provide long spills of particles by employing resonant extraction where the circulating beam is slowly ejected over thousands to millions of turns by exploiting the amplitude growth caused by a transverse resonance. In the CERN Super Proton Synchrotron (SPS), this method is used to satisfy the experimental requests of the North Area. However, the extracted particle flux is modulated by power-converter ripple, an issue shared across all sychrotrons that perform resonant extraction. In order to suppress such modulations, empty-bucket techniques can be employed, which take advantage of chromaticity to quickly accelerate particles into resonant motion by using a longitudinal rf system. This paper explores empty-bucket techniques via theory, simulation, and measurement, providing a systematic characterization with general applicability to any machine. Additionally, the operational implementation in the SPS is detailed, where the impact on the beam profile and extracted intensity is addressed.

DOI: 10.1103/PhysRevAccelBeams.27.074001

I. INTRODUCTION

The North Area (NA) is a fixed-target experimental area located at CERN, which receives 400 GeV proton spills of length $T = 4.8$ s from the Super Proton Synchrotron (SPS) along with ion beams of various species and energies. To fulfill this request, the SPS exploits third-integer resonant extraction to slowly empty the circulating beam into the transfer line. The process relies on synchronously ramping all magnetic elements in the lattice, so as to push the coasting beam's horizontal transverse tune Q toward the resonant value of $\frac{80}{3}$ while keeping the beam optics unchanged [1].

In an ideal scenario, the extracted flux $I(t)$ would have a rectangular shape with value I_0/T where $t \in [0, T]$ and zero otherwise. I_0 corresponds to the total extracted intensity. However, undesired noise is practically unavoidable, and one may compute the relative magnitude $\hat{I}(f_i)$ of a given spectral perturbation as follows:

$$\underline{I}(f_i) = \left|\frac{I(f_i)}{I_0}\right| = \left|\frac{\int_T I(t)\exp(-i2\pi f_i t)dt}{\int_T I(t)dt}\right|, \quad (1)$$

where f_i is the frequency of the perturbation.

In the SPS, pronounced peaks can be observed at harmonics of 50 Hz (e.g., 50, 100, 150 Hz), generally arising from the imperfect ac-to-dc rectification of the main-grid current. This will affect the magnetic field of the focusing and bending fields and, ultimately, the instantaneous extracted flux. Such variations, if too large in amplitude, lead to unmanageable rates that saturate the buffers of the NA experiments, resulting in the loss of valuable data [2]. In fact, the problem of noise or ripple on slowly extracted spills is a general concern across most synchrotrons, and a variety of approaches have been developed over the years to reduce its impact.

A general ripple-suppression concept is that of modifying the beam dynamics of the slow-extraction process itself so as to make the system less sensitive to the perturbations caused by ripple. Techniques of this sort usually have the downside of affecting other aspects of the extraction (such

*pablo.arrutia@cern.ch
Also at University of Oxford, United Kingdom.

as beam loss) but can be very powerful if successfully integrated within the relevant constraints. For example, one may increase particles' tune speed when crossing the resonance boundary. This may be achieved by optimizing the chromaticity [3] or by acting on the beam's longitudinal trajectories using rf cavities [4,5], among others. For a chromatic (momentum-driven) extraction like that of the SPS, the extracted flux can be approximately expressed as

$$I(t) = -\rho \left.\frac{dQ}{dt}\right|_{Q=\frac{80}{3}} = -\rho \left[\dot{Q} + \sum_i 4\pi f_i a_i \sin(2\pi f_i t + \phi_i)\right]\Bigg|_{Q=\frac{80}{3}}, \quad (2)$$

where $\rho = \frac{\partial n}{\partial Q}$ is the distribution of tunes in the ring, $\dot{Q}$ is the average tune speed, and a_i, f_i, ϕ_i are the ith ripple amplitude, frequency, and phase, respectively. All quantities are evaluated at $Q = \frac{80}{3}$, i.e., the boundary between stable and unstable transverse motion. Equation (2) can be substituted into Eq. (1) to obtain

$$\underline{I}(f_i) = \frac{a_i \pi f_i}{\dot{Q}}. \quad (3)$$

Simply put, the ripple-reduction coefficient G achieved by a new system with respect to a reference system is,

$$G(f_i) = \frac{I_{\text{new}}(f_i)}{I_{\text{ref}}(f_i)} = \frac{1}{K}, \quad (4)$$

where $K = \frac{\dot{Q}_{\text{new}}}{\dot{Q}_{\text{ref}}}$ is the speed-up factor across the resonance boundary.

Additionally, upon entering the resonance, particles with different initial conditions may take different transit times τ to move far from the instability boundary and reach the septum. This spread in transit times $\Delta\tau \propto \text{Mean}(\tau)$ leads to a low-pass filter effect with cutoff frequency $f_c \propto 1/\Delta\tau$ [6]. In the SPS, the tune-to-spill transfer function can be modeled as a second-order low-pass filter with f_c at approximately 100 Hz [3,7]. Several efforts have shown that spill quality can be improved by modifying this transit-time spread [3,8]. In general, the propagation of tune ripple to spill ripple can be characterized by a transfer function $\hat{I}$:

$$\hat{I}(f_i) = \frac{\underline{I}(f_i)}{a_i}. \quad (5)$$

For small ripple ($a_i \pi f_i < \dot{Q}$ for a single spectral component), $\hat{I}(f_i)$ is independent of a_i, i.e., the process can be modeled as a linear system [3].

This paper studies empty-bucket techniques that exploit the acceleration provided by an rf cavity to modify the transverse beam dynamics during slow extraction. This relies on the chromatic coupling of the machine, which converts the change in longitudinal momentum caused by the cavity voltage into a change in transverse tune via chromaticity. Thus, the technique fits well with the current operation in the SPS, since the machine already relies on a momentum-driven extraction method, and the rf systems conventionally employed for acceleration can easily accommodate the implementation. Empty-bucket channeling (EBC) was first proposed and implemented in the CERN Proton Synchrotron (PS) in 1981 [9] based on the method of phase-displacement acceleration used in the Intersecting Storage Rings [10]. Since then, EBC has been utilized in a few facilities [11,12] for spill-quality improvement. The technique has also been studied for the provision of slow-extracted bunched beams via both simulation and measurement [13,14].

With regard to spill-quality improvements, however, all implementations have remained mostly empirical and no systematic studies are available in the literature. In order to complement and expand upon such efforts, this paper provides a comprehensive exploration by combining theory, simulation, and measurement. The goal is to understand the impact of different parameters, build a computational model that can be exploited to make predictions, and, ultimately, show how the acquired insights can be used to operationally deploy the technique in a real machine. In fact, it is shown that in certain circumstances, the technique can be operated outside the conventional channeling regime and still obtain substantial ripple suppression. The paper also details the operational implementation of the SPS, with particular focus on the relevant constraints.

II. SPILL SIMULATION MODEL FOR THE SPS

Recent tracking studies of the SPS have shown that Henon-map approaches—where the lattice is modeled by a linear matrix and a single thin sextupole—perform impressively in spill-quality studies. They can display an agreement with measurement comparable to that of a MADX model including the full lattice, but at a hundredth of the computational cost [15]. Note, however, that in smaller machines with less elements, the speed-up would be more modest. In the PS, similar models have been utilized successfully for the study of novel rf manipulations [16,17].

Following the same trend, this paper reduces the SPS extraction dynamics to the following four mapping equations (with the SPS lattice parameters shown in Table I):

$$\begin{aligned} X_{n+1} &= X_n \cos 2\pi Q_n + X'_n \sin 2\pi Q_n \\ X'_{n+1} &= -X_n \sin 2\pi Q_n + X'_n \cos 2\pi Q_n + S X_n^2 \\ \phi_{n+1} &= \phi_n - 2\pi h \eta (\delta_n - \delta_{\text{rf}}) \\ \delta_{n+1} &= \delta_n + \frac{eV}{\beta^2 E}(\sin\,\phi_n - \Gamma), \end{aligned} \quad (6)$$

TABLE I. SPS nominal parameters.

Quantity	Symbol	Value
Beam energy (GeV)	E	400
Revolution frequency (kHz)	f_0	43.4
Relativistic energy factor (1)	γ	426.4
Chromaticity (1)	Q'	−26.67
Virtual-sextupole strength ($m^{-1/2}$)	S	170
Slip factor (1)	η	0.00184
Energy change per turn (kV)	ΔE	4
Geometric emittance (mm mrad)	ϵ	23.5×10^{-3}
Beam's central δ offset (1)	⋯	1.2×10^{-3}
Beam's total δ spread (1)	⋯	2×10^{-3}

where the variables X, X' represent the normalized position and angle (horizontal phase space), and ϕ, δ represent the phase and relative-momentum offsets, respectively (longitudinal phase space). Furthermore, the rf cavity is characterized by its voltage V, its frequency offset δ_{rf} (in units of relative-momentum offset), and its harmonic h. The sine of the unstable phase, $\Gamma = \Delta E/eV$, captures the energy change per turn, which is caused by the synchronous ramp up of the SPS magnetic rigidity $B\rho$. Although the beam's energy does not physically change (unlike in betatron-core extraction), particles still "see" an accelerating bucket characterized by

$$\Delta E = 2\pi\, Re \frac{d(B\rho)}{dt} \quad \text{or} \quad \Gamma = \frac{2\pi R}{V}\frac{d(B\rho)}{dt}, \tag{7}$$

where $2\pi R = \beta c/f_0$ is the circumference of the accelerator.

As a consequence of the ramp, in COSE-driven extraction, one has to additionally ramp the rf frequency f_{rf} in synchrony with the rigidity to keep δ_{rf} constant over time. In the case of the SPS, this effect is small due to its high relativistic γ and can be safely ignored [18].

To simulate extraction, a particle is considered to leave the ring when $X > X_{ZS}$, where X_{ZS} is the horizontal distance from the closed orbit to the septum blade. In addition, spill perturbations are modeled by updating the tune turn by turn:

$$Q_n = \frac{80}{3} + Q'\delta_n + \sum_i 2a_i \sin 2\pi \frac{f_i}{f_0} n. \tag{8}$$

This approach has been borrowed from [3] and relies on the fact that slow extraction is most sensitive to tune perturbations, even though magnetic ripple will also have an effect on other parameters (e.g., closed orbit or chromaticity). These additional effects can be treated as higher-order corrections on the extracted flux and are thus ignored in this paper.

III. CONCEPTUAL ASPECTS OF EMPTY-BUCKET TECHNIQUES

During nominal fixed-target operation in the SPS, the beam is accelerated to flattop by the main rf system ($h = 4620$) while using the auxiliary rf system ($h = 18\,480$) to tame longitudinal instabilities. Once at flattop, the total rf voltage is set to zero and the beam debunches to cover the whole ring. At this point, the magnetic ramp is initiated and the coasting beam is pushed toward the resonance. One of the rf systems must be turned back on before the start of the magnetic ramp, which will be involved in the empty-bucket manipulation. In order to avoid recapturing the coasting beam, an offset must be added to the rf frequency before turning on the voltage.

The process of EBC, as envisioned in its original implementation [9], is shown in Fig. 1. Note that, since the SPS extracts with nonzero chromaticity (a necessary requirement for COSE to work), the relative-momentum offset δ can be used to quantify both the beam's distance to the rf buckets (longitudinally) and the distance to the tune resonance (horizontally). EBC can be used to increase the tune speed selectively to achieve large K only near the resonance boundary, without affecting the total spill length [19]. For the technique to work, the rf frequency and the horizontal resonance must be aligned with respect to each other. This is achieved when the following relationship is approximately satisfied:

$$\delta_{\mathrm{rf}} = \pm\delta_r = \pm\frac{\sqrt{\epsilon}S}{(48\sqrt{3}\pi)^{1/2}Q'}, \tag{9}$$

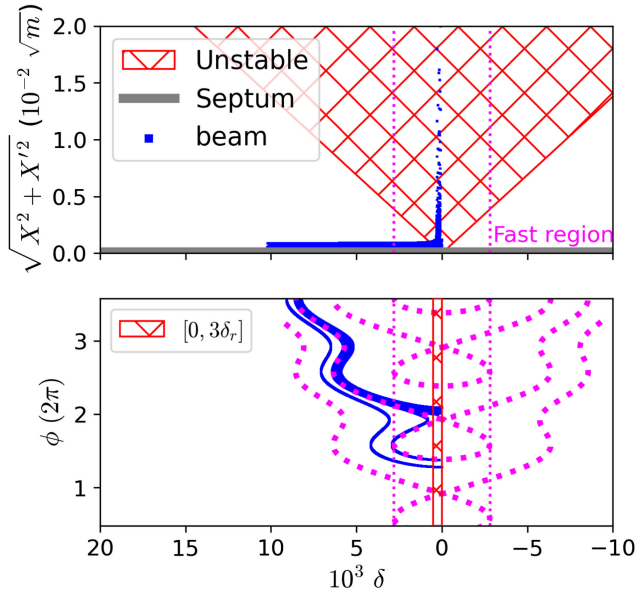

FIG. 1. Simulated particle trajectories (blue) undergoing empty-bucket channeling. The empty buckets (fuchsia, bottom) constrain trajectories within narrow channels in longitudinal phase space, which results in a "fast region" that particles travel through as they enter the unstable region (top).

where δ_r is known as the resonance stop band, and the $\pm$ sign depends on whether the initial beam starts with positive/negative momentum offset. For the rest of this paper, the positive sign will be assumed, as it matches the extraction scheme in the SPS.

A. Small-offset implementation

In [19], Crescenti provided a formula for K, where it was shown that a particle with transverse amplitude equal to $\sqrt{\epsilon}$ will experience a speed-up given by

$$K_1 = 1 + \frac{1}{\Gamma} \cdot \left[\frac{\cos\phi_r - \cos\phi_l}{\phi_r - \phi_l} \right], \tag{10}$$

where ϕ_l, ϕ_r delimit the channel width as shown in Fig. 2 and must be numerically found for a given momentum offset within $\delta_{RF} \in [\delta_r, \hat{\delta}_b + \delta_r]$. The formula is often interpreted geometrically with the help of Liouville's theorem: as the available phase space is constrained within narrow channels, the incompressible beam distribution speeds up to preserve its phase-space density. Equation (10) describes precisely the δ-direction component of the average phase-space speed (if a uniform beam distribution is assumed between ϕ_l and ϕ_r).

For a large rf offset, the acceleration from the sinusoidal rf voltage is averaged over all phases providing no net speedup ($K_1 = 1$). In fact, this happens when the offset is larger than one bucket height, i.e., $|\delta_{\rm rf} - \delta_r| > \hat{\delta}_b$ with

$$\hat{\delta}_b = 2\sqrt{\frac{eV}{2\pi\beta^2 Eh|\eta|}} Y(\Gamma) = \hat{\delta}_{b,0} Y(\Gamma), \tag{11}$$

being the rf-bucket height and $Y(\Gamma)$ is the bucket-height factor [20].

B. Large-offset implementation

The previous subsection assumes that particles are uniformly distributed between ϕ_l and ϕ_r, which leads to no speedup once the bucket is offset from the resonance by one bucket height. However, this is not exactly the case, as illustrated in Fig. 3. Particle trajectories start with $\delta > \delta_r$ and, therefore, preferentially enter the resonance with initial phases for which the rf kick points toward the resonance. Additionally, particles are not immediately extracted upon entering the resonance, and the effects from the rf kicks will perturb their transverse trajectories and, potentially, their transit times.

Actually, the fact that the presence of an empty bucket still provides ripple suppression even when $|\delta_{\rm rf} - \delta_r| > \hat{\delta}_b$ has been empirically observed [21] and will be confirmed throughout this paper. It is important to note that, unlike in the small-offset implementation, in this configuration, particles never travel between empty buckets, as they are extracted before they can reach the channels. Indeed, particles simply follow quasiperiodic momentum oscillations as they approach the resonant momentum. For this reason, we will refrain from using the expression "empty-bucket channeling" to describe this scenario. Instead, we

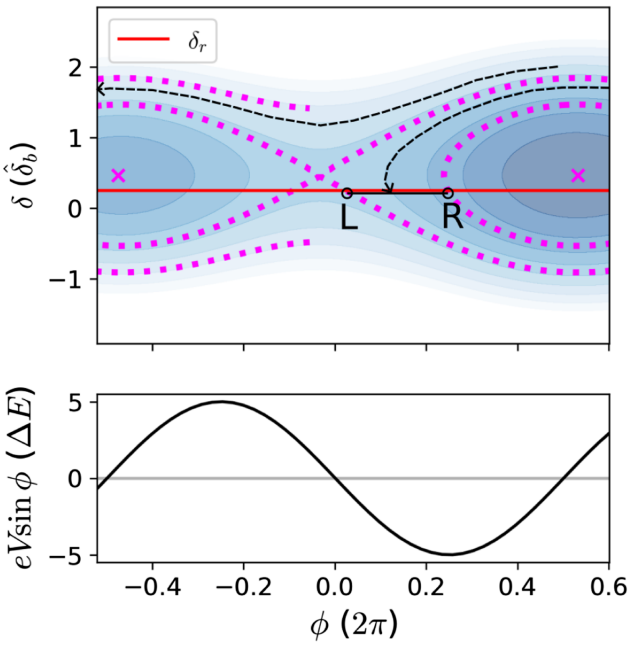

FIG. 2. Illustration of "small-offset" EBC: particle trajectories (dashed black) reach the resonant momentum δ_r while constrained within a narrow channel of phases (between points L and R). These particles only sample voltages that push them toward the resonance (bottom).

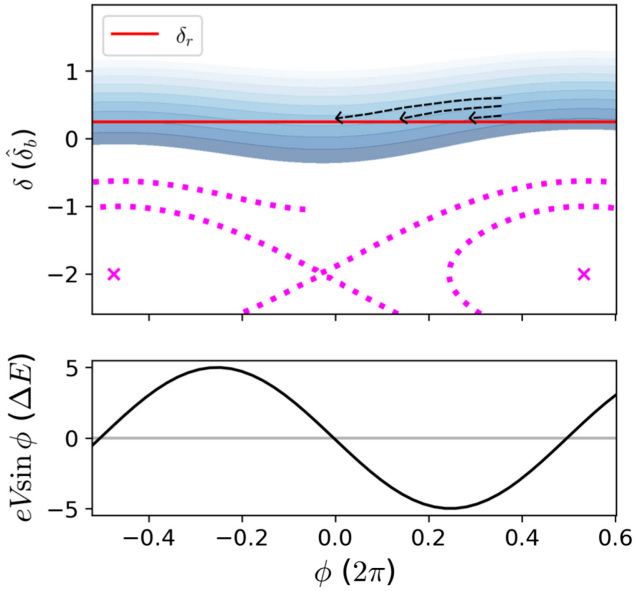

FIG. 3. Illustration of large-offset EBC: particle trajectories (dashed black) reach the resonant momentum δ_r aided by the momentum oscillations caused by the rf-voltage kicks (bottom). Particles preferentially reach the resonance when the kicks point toward the resonance.

will make the distinction between "small-offset" empty bucket and "large-offset" empty bucket (EB).

This subsection provides a simple heuristic study to characterize the phenomenon of large-offset EB. We start by replacing the longitudinal difference equations from Eq. (6) with their respective differential approximations, where the revolution period is taken as the fundamental unit of time:

$$\frac{d\phi}{dt} = -2\pi h\eta f_0(\delta - \delta_{\mathrm{rf}}), \qquad \frac{d\delta}{dt} = \frac{eVf_0}{\beta^2 E}(\sin\phi - \Gamma). \tag{12}$$

For large momentum offsets, we may substitute $\delta - \delta_{\mathrm{rf}} = \delta_{\mathrm{rf}} + \delta_1$ (with $|\delta_1| \ll |\delta_{\mathrm{rf}}|$) in Eq. (12) to obtain the following first-order approximation,

$$\delta_1(t) = A\cos\left(\frac{2\pi}{T_s}t - \phi_0\right) - \frac{\Delta E}{\beta^2 E}f_0 t, \tag{13}$$

with the excitation amplitude A given by

$$A = \frac{\hat{\delta}_{b,0}^2}{4|\delta_{\mathrm{rf}}|} \tag{14}$$

and the excitation period T_s given by

$$T_s = \frac{1}{h|\eta\delta_{\mathrm{rf}}|f_0}. \tag{15}$$

It can be seen that the momentum dynamics follow quasisinusoidal oscillations, similar to those of linearized synchrotron motion. Thus, it is not surprising that this regime can exhibit ripple suppression, as it has been previously observed for conventionally bunched beams [22]. The phenomenon can be understood via the mechanism of "tune wobbling" [8]: as particles oscillate in tune, they may exit and reenter the unstable region several times before being extracted, which will impact the transit-time spread. To achieve this, the excitation amplitude A must be larger than the ripple amplitude a_i (in units of tune). Additionally, $1/T_s$ is typically chosen to be larger than f_c, so as to avoid strongly modulating the spill. However, unlike in quadrupole-driven tune wobbling, the oscillations during large-offset EB are not in phase between particles coasting at different longitudinal phases, mitigating the coherent spill ripple at $f_i = 1/T_s$. This in turn means that $1/T_s$ need not be chosen beyond the cutoff frequency f_i. Sections V B and V C will provide additional details on how A and T_s affect ripple suppression, further characterizing the tune-wobbling mechanism through large-offset EB.

IV. EFFECTS ON TUNE SPEED AND TRANSIT TIME

The previous section has described two mechanisms by which empty-bucket techniques lead to ripple suppression: tune speedup and impact on transit times. In this section, simulations were conducted employing the simple model from (6) to showcase these two effects both for the small-offset and the large-offset implementations. In order to do so, three configurations were selected: (i) EB off; (ii) EB on with $\delta_{\mathrm{rf}} = 0$, i.e., small-offset regime; and (iii) EB on with $\delta_{\mathrm{rf}} = 3\hat{\delta}_b$, i.e., large-offset regime. For the cases with EB on, the rf harmonic and the rf voltages were fixed to $h = 18\,480$ and $eV = 50\Delta E = 200$ keV, respectively, which will later be used for the operational implementation in Sec. VII.

Figure 4(a) shows the longitudinal-phase distributions of the extracted particles for each of the configurations. The conventional small-offset implementation produces a nonuniform distribution that results in nonuniform sampling of the rf waveform and, as a consequence, tune speedup. On the contrary, the large-offset implementation only produces a mild modulation, which is insufficient to significantly improve spill quality through tune speedup. However, the improvement for the large-offset implementation can be explained by the increase in effects on the transit-time spread, as shown in Fig. 4(b). It must be noted that the small-offset implementation also has an impact on the transit times, albeit much smaller than that of the large-offset implementation. This can be explained by the fact that some particles need to traverse the resonance several times before being extracted [19], visible as a long tail on the transit-time distribution.

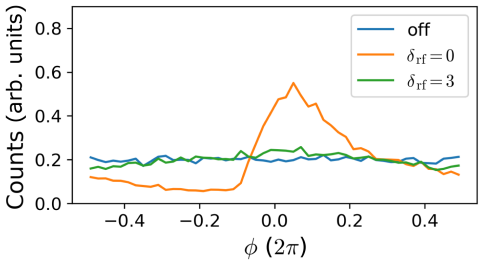

(a) Longitudinal phase ϕ

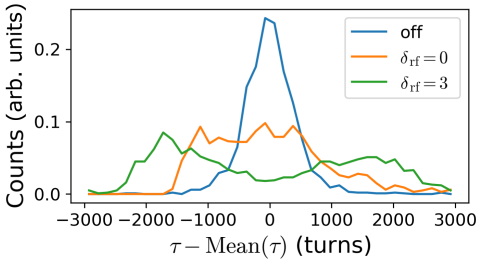

(b) Transit time τ

FIG. 4. Simulated longitudinal-phase and transit-time distributions of extracted particles for three configurations: (i) EB off, (ii) EB on with $\delta_{\mathrm{rf}} = 0$, $h = 18\,480$, $eV = 50\Delta E$, and (iii) EB on with $\delta_{\mathrm{rf}} = 3$, $h = 18\,480$, $eV = 50\Delta E$. δ_{rf} is given in units of $\hat{\delta}_b$.

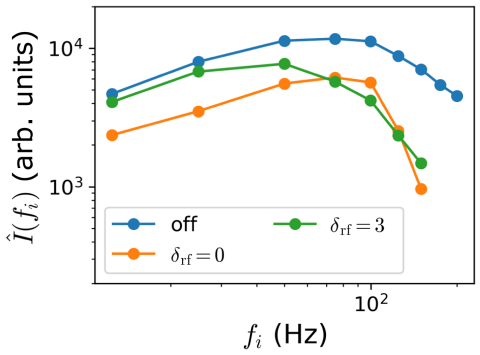

FIG. 5. Simulated tune-ripple to spill-ripple transfer function $\hat{I}(f_i)$ for three configurations: (i) EB off, (ii) EB on with $\delta_{\rm rf}=0$, $h=18\,480$, $eV=50\Delta E$, and (iii) EB on with $\delta_{\rm rf}=3$, $h=18\,480$, $eV=50\Delta E$. δ_{rf} is given in units of $\hat{\delta}_b$.

To further quantify these phenomena, Fig. 5 shows the simulated tune-ripple to spill-ripple transfer function $\hat{I}$ as a function of ripple frequency f_i for the same three configurations. When compared to the "EB off" case, the small-offset transfer function exhibits a lower gain and a sharper roll-off after the cutoff frequency. These characteristics are consistent with a faster tune speed and a longer tail in the transit-time distribution, respectively. The large-offset implementation, on the other hand, produces little impact on the gain but significantly reduces f_i, as expected. In general, EB techniques will suppress ripple through a combination of tune speed-up and transit-time impact.

V. RIPPLE-SUPPRESSION SIMULATION STUDIES

The simple model from Eq. (6) is now employed to systematically characterize the behavior of EB techniques as a function of different relevant parameters, namely rf harmonic, ripple frequency, rf voltage, and rf-frequency offset. Even though we will be using the SPS parameters listed in Table I, the ultimate aim of the characterization is to provide a machine-independent understanding of EB techniques and to list general criteria for optimization.

For a real implementation in the machine, the simplest characterization procedure is to fix the rf voltage V and harmonic h while scanning the rf frequency $\delta_{\rm rf}$. Then, one observes the ripple-suppression coefficient G for a spill perturbation of a given frequency f_i. For this reason, the studies in this section will be displayed as scans in $\delta_{\rm rf}$ for different choices of h, V, and f_i. Additionally, characterizations in terms of T_s and A will also be provided, in an attempt to expand upon the tune-wobbling phenomenon.

A. Dependence on rf harmonic

As a first step, one must select the rf system to employ. The SPS rf system, for example, is equipped with cavities at both $h=4620$ and $h=18\,480$. To characterize $G(f_i|h,\delta_{\rm rf})$, both the cavity harmonic and the rf frequency were scanned, while the cavity voltage was fixed to 200 kV ($eV=50\Delta E$) and the input spill-ripple frequency was set to 100 Hz. The spill-ripple magnitude was then normalized to a reference value (rf off) to obtain $G(f_i=100\ \text{Hz}|h,\delta_{\rm rf})$.

Figure 6 shows the outcome of the simulation study, where the rf-frequency offset has been normalized by the rf bucket height $\hat{\delta}_b$. Regardless of the rf harmonic, the suppression is maximal when the rf bucket overlaps with the resonant stop band, as this ensures that particles crossing the stability boundary are being channeled between buckets. However, lower harmonics still provide substantial ripple suppression when this overlap condition is not fulfilled.

Figure 7 further demonstrates the difference between low and high harmonics by showing two cross sections of Fig. 6 at constant h and varying $\delta_{\rm rf}$. The suppression factor predicted by $1/K_1$ [Eq. (10)] provides good agreement with the simulation. All in all, the prescription derivable from this subsection is the following: all other things equal, low harmonic implementations of EB techniques are more robust, as they provide a wider ripple-reduction valley even when normalized by their larger bucket height. In the SPS, this would imply implementing the technique with the main system ($h=4620$) rather than with the auxiliary system ($h=18\,480$). However, an implementation with the $h=4620$ system is hard to realize in nominal operation. The reason for this is that the main rf system is already employed during the first 800 ms of extraction to speed up the debunching process through a feedback loop. It would be technically very challenging to overload the same system to perform EBC on top of this, effectively coupling the two tasks from a control standpoint. Therefore, the simulations in the following subsections will be performed with $h=18\,480$, with the idea of employing the auxiliary

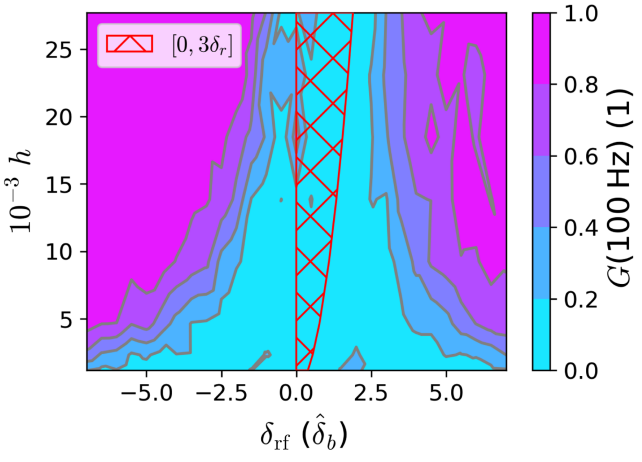

FIG. 6. Simulated ripple-reduction coefficient G vs rf offset $\delta_{\rm rf}$ and rf harmonic h. The rf voltage and ripple frequency were kept fixed at 200 kV and 100 Hz, respectively.

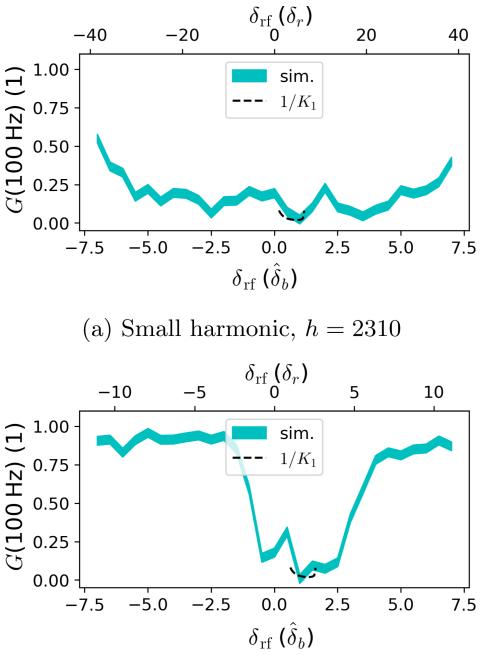

(a) Small harmonic, $h = 2310$

(b) Large harmonic, $h = 27720$

FIG. 7. Simulated ripple-reduction coefficient G vs rf offset $\delta_{\rm rf}$ for two different rf harmonics. The rf voltage and ripple frequency were kept fixed at 200 kV and 100 Hz, respectively.

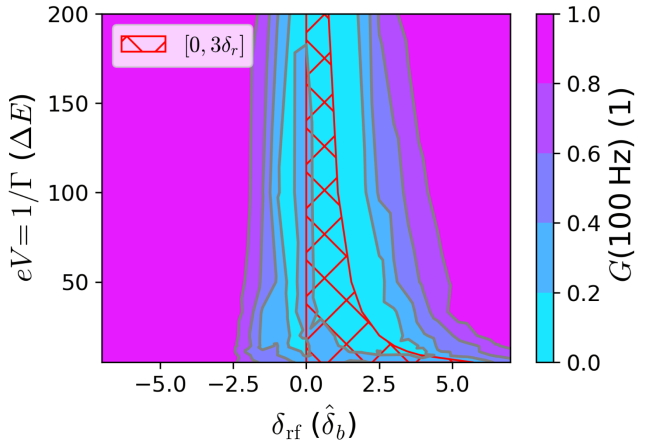

FIG. 8. Simulated ripple-reduction coefficient G vs rf offset $\delta_{\rm rf}$ and rf voltage V. The rf harmonic and ripple frequency were kept fixed at 18 480 and 100 Hz, respectively.

rf system in an operational implementation of EBC. Regardless, the general trends discussed should be somewhat independent of h.

B. Dependence on rf voltage

Once h has been fixed, one must select a voltage. The study in this section fixes $h = 18\,480$ (and maintains $f_i = 100$ Hz as before), while scanning V and $\delta_{\rm rf}$ to characterize $G(f_i = 100\ \mathrm{Hz}|V, \delta_{\rm rf})$. Figure 8 shows the simulation output of the scan when V is varied in the range $(10\Delta E, 200\Delta E) = (40\ \mathrm{kV}, 800\ \mathrm{kV})$. The plot demonstrates that substantial suppression can be achieved even when using a small V. Moreover, the suppression-region width is essentially independent of V when $\delta_{\rm rf}$ is normalized by $\hat{\delta}_b \propto \sqrt{V}$ for regions where $\hat{\delta}_b \gg \delta_r$.

In order to better understand the contours of equal G, it is useful to reexpress V and $\delta_{\rm rf}$ in terms of A and T_s, focusing only on large-offset EB. Figure 9 shows the outcome of a simulation study where G has been computed for $f_i = 50$ Hz, 100 Hz as a function of A and T_s. Only $\delta_{\rm rf} > \hat{\delta}_b$ is shown, but similar functional dependencies were obtained for $\delta_{\rm rf} < -\hat{\delta}_b$. The plots confirm the observations from [8] that the excitation amplitude must exceed the ripple amplitude in order to achieve substantial ripple suppression. Additionally, it can be seen that for each f_i an optimal $f_{\rm opt} = 1/T_s$ exists, for which a smaller A is needed to obtain certain ripple-reduction factor G. Then, as $1/T_s$ moves away from the optimum (either toward smaller or larger frequencies), A must be increased accordingly to maintain G. If one takes $1/G$ to be the response of a system to a perturbation, the phenomenon is analogous to the behavior of a damped resonant system with resonant frequency $f_{\rm opt}$. This is not surprising since we are effectively introducing a "deliberate" tune ripple, which should be amenable to the same transfer-function approach explored in [3] for undesired tune ripple. It is interesting

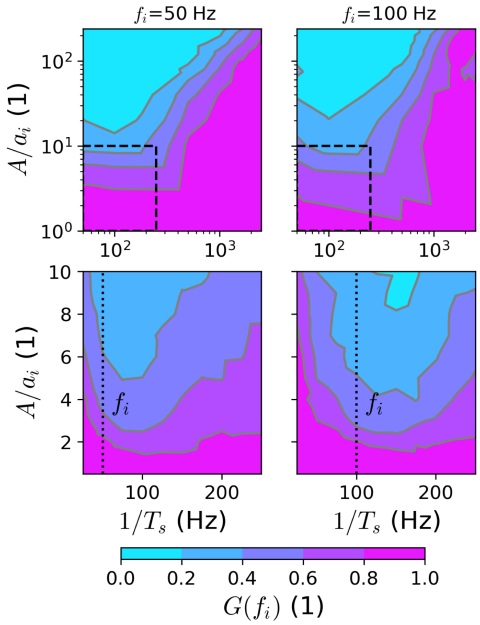

FIG. 9. Simulated ripple-reduction coefficient G vs excitation frequency $1/T_s$ and excitation amplitude A (normalized to ripple amplitude a_i) for two different ripple frequencies f_i. Each lower plot shows the detailed output of its respective upper plot within the dashed region. The rf harmonic was kept fixed at 18 480.

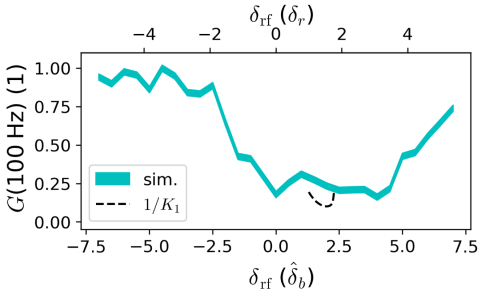

(a) Small voltage, $eV = 9\Delta E$

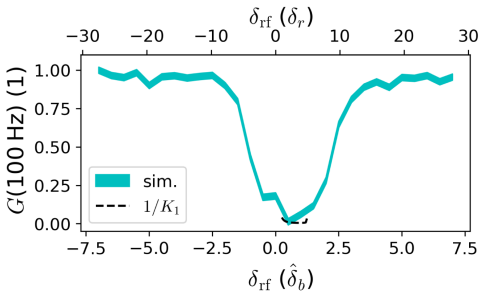

(b) Large voltage, $eV = 200\Delta E$

FIG. 10. Simulated ripple-reduction coefficient G vs rf offset δ_{rf} for two different rf voltages. The rf harmonic and ripple frequency were kept fixed at 18 480 and 100 Hz, respectively.

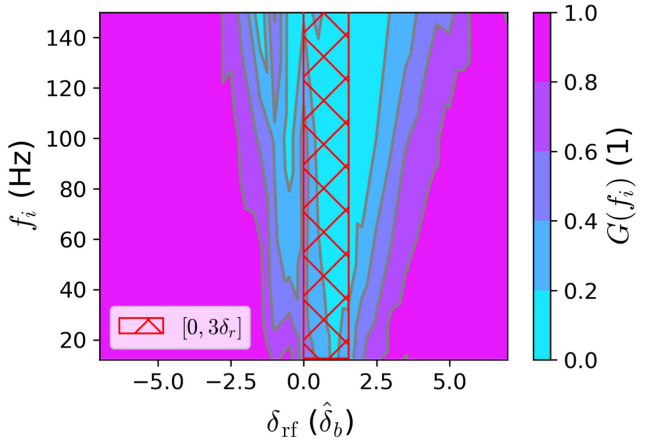

FIG. 11. Simulated ripple-reduction coefficient G vs rf offset δ_{rf} and ripple frequency f_i. The rf voltage and harmonic were kept fixed at 200 kV and 18 480, respectively.

to note that $1/T_s$ can be smaller than the ripple frequency (and the cutoff frequency) and still achieve ripple suppression. Such a configuration would introduce a coherent strong modulation for quadrupole-driven tune wobbling, but this is not the case for large-offset EB as modulations are out of phase between different particles in the coasting beam.

Finally, Fig. 10 shows two cross sections of constant voltage and varying rf-frequency offset. This plot confirms that the width of the suppression valley (in units of $\hat{\delta}_b$) is wider for the small-voltage case. Furthermore, it can be seen that the analytical estimate $1/K_1$ provides a good approximation for small-offset EB, but simulations are necessary in order to explore the wider suppression valley provided by large-offset EB.

With regard to the choice of voltage, we can conclude that small voltages will typically be sufficient to significantly improve the operational spill quality. While it is true that higher voltages lead in theory to higher suppression, in practice, one may be constrained by other effects. In the SPS, for example, the large voltages can introduce strong perturbations in the transverse dynamics through chromatic coupling, which can lead to significant beam loss caused by emittance blowup of the extracted beam [23,24]. This effect is shown in more detail in Sec. VII B.

C. Dependence on ripple frequency

Once h and V have been chosen, the ripple-suppression potential across different ripple frequencies can be studied, i.e., $G(f_i|\delta_{\mathrm{rf}})$. Indeed, the previous subsections have already characterized $G(f_i = 100\ \mathrm{Hz})$, but we must not forget that one of the main appeals of EB techniques is their broadband suppression capabilities.

In a similar fashion to previous subsections, Fig. 11 shows the outcome of a simulation study where $h = 18\,480$, $V = 200$ kV (eV $= 50\Delta E$), and f_i and δ_{rf} are varied. The maximum f_i has been restricted to 150 Hz, which is already well beyond the SPS cutoff frequency $f_c \approx 100$ Hz. It can be observed that the suppression valley is wider for larger ripple frequencies. As already demonstrated in Sec. IV, EB techniques can affect both the transfer function's shape (i.e., cutoff frequency and filter order), as well as its overall gain. The former effect will potentially result in different ripple suppression for different frequencies.

Two cross sections of constant f_i and varying δ_{rf} are shown in Fig. 12, again demonstrating that $1/K_1$ serves as a good estimate for G within the small-offset region. Additionally, Fig. 12(b) shows a pronounced local maximum in the G-curve at $\approx\delta_{\mathrm{rf}} = -\hat{\delta}_b$. For that particular momentum offset, resonant particles travel near the bucket separatrix, which results in a long T_s and no substantial speedup as the channel is not reached. In other words, this setup is not optimized either for small-offset EB or for large-offset EB. For this configuration, the same feature is not visible in the G curve for $f_i = 12$ Hz [Fig. 12(a)].

Informed by these observations, we conclude that the EB configuration chosen for the SPS is a more robust choice for mitigating the effects of ripple at higher frequency. Of course, this is not to say that it is ineffective against slower ripple but that the empty bucket must be aligned with higher precision, which will make it inconvenient in machines where shot-to-shot jitter is non-negligible. For example, the SPS suffers from magnetic-history effects

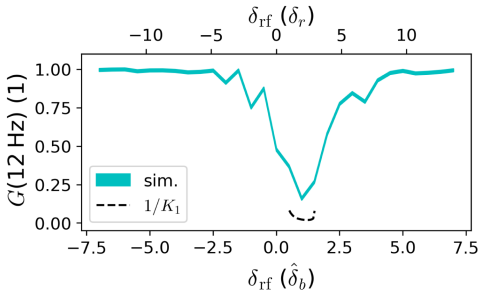

(a) Small frequency, $f_i = 12$ Hz

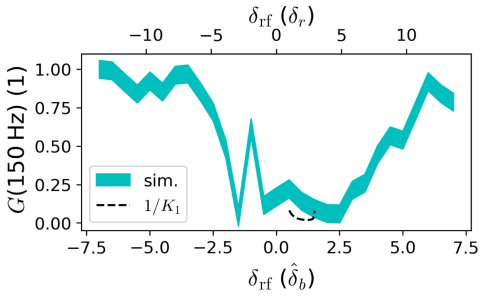

(b) Large frequency, $f_i = 150$ Hz

FIG. 12. Simulated ripple-reduction coefficient G vs rf offset δ_{rf} for two different ripple frequencies. The rf voltage and harmonic were kept fixed at 200 kV and 18 480, respectively.

when switching between supercycles, which shifts the resonant momentum of the machine at flattop.

We conclude this subsection by further studying large-offset EB within the context of tune wobbling. To do so, a simulation study was conducted to characterize G as a function of f_i and $1/T_s$ for four different values of A. The outcome of the study is shown in Fig. 13. It can be seen that for the smallest excitation amplitude ($A/a_i = 2$), a mild ripple suppression can be achieved across all f_i, provided that $1/T_s$ is optimally tuned. Then, as A/a_i is increased, the suppression valley deepens and widens. Again, the analogy with damped resonant systems is useful: for a small excitation amplitude, the system must be driven close to its resonant frequency to produce a substantial response; for a larger excitation amplitude, this constraint is relaxed.

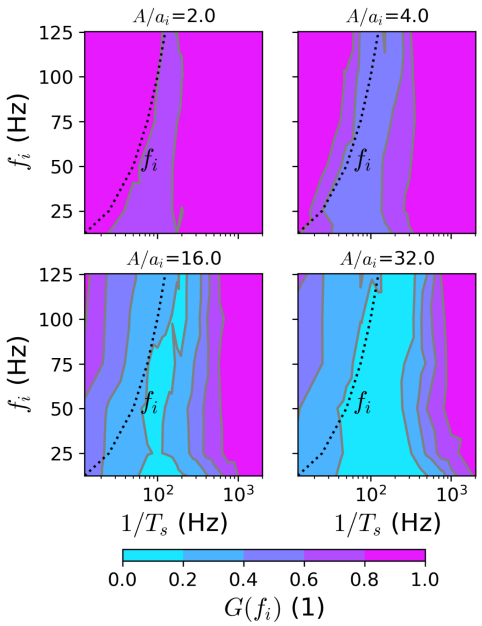

FIG. 13. Simulated ripple-reduction coefficient G vs excitation frequency $1/T_s$ ripple frequency f_i for four different excitation amplitudes A (normalized to the ripple amplitude a_i). The rf harmonic was kept fixed at 18 480.

VI. BENCHMARKING WITH MEASUREMENTS

The previous section has provided a thorough characterization of EB techniques in terms of the relevant rf and spill-ripple parameters by exploiting a simple simulation model. The characterization has also been compared to semianalytical estimation $1/K_1$, and a qualitative understanding has been developed for the different dependencies. However, direct comparison with measurement is crucial to verify the predictive validity of the model.

To do so, two scenarios were implemented and investigated in the SPS machine: (a) Implementation with the main "200 MHz system" ($h = 4620$). The voltage was fixed at 50 kV (eV $= 12.5\Delta E$). (b) Implementation with the auxiliary "800 MHz system" ($h = 18\,480$). The voltage was fixed at 200 kV (eV $= 50\Delta E$). The voltages chosen for each system are close to the minimum that their respective control systems can provide. This choice was made with a future operational implementation in mind, trying to minimize perturbations to the beam that could increase beam loss during the extraction process.

For each setting, the frequency offset of the cavity was scanned, and the resulting spill time structure was recorded at the NA62 experiment by employing their GTK detector [25]. The amplitudes of the 50 and 100 Hz components were extracted via spectral analysis and normalized to a reference value recorded with rf off to compute G. The predictions of the simulation model and $1/K_1$ were likewise computed for each measurement setting.

Figure 14 shows the outcome of the study. The measurements verify that EB techniques can strongly suppress the undesired ripple in the SPS even when employing the minimum voltage allowed by the cavity control system. Furthermore, the simulation predictions are in good agreement with measurements across the entire dataset investigated, reliably reproducing the dependencies with regard to rf harmonic, rf voltage, and ripple frequency as a function of rf-frequency offset. The simulation even reproduces the local maximum in the G curve that is visible for the $h = 18\,480$ case, a phenomenon highlighted in the previous section. In practice, this feature demonstrates that $G(f_i|\delta_{\mathrm{rf}})$ is not necessarily a convex function.

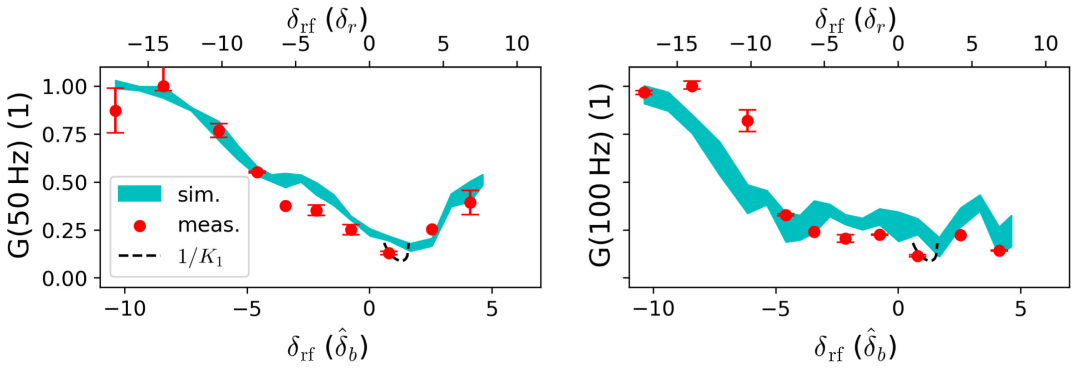

(a) $h = 4620$, $V = 50\,\mathrm{kV}$ ($eV = 12.5\Delta E$)

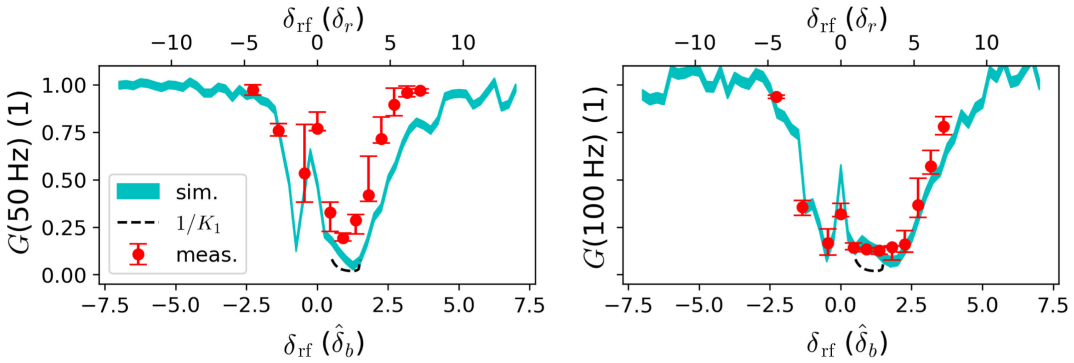

(b) $h = 18480$, $V = 200\,\mathrm{kV}$ ($eV = 50\Delta E$)

FIG. 14. Measured ripple-reduction coefficient G vs rf offset δ_{rf} for two different rf harmonics ($h = 4620$, 18 480) and two different ripple frequencies ($f_i = 50, 100$ Hz). The error bars show the shot-to-shot variability.

VII. OPERATIONAL IMPLEMENTATION AT THE SPS

The promising results from the measurement test provided a strong motivation to pursue an operational implementation of EB techniques in the SPS, especially given the negative impact of the 100 Hz ripple on the data acquisition system of the NA62 experiment. This section documents such implementation with a particular focus on the constraints to keep in mind, which are somewhat general irrespective of the specific machine.

As mentioned before, the $h = 4620$ rf system is already used during the first 800 ms of extraction to aid with the beam's debunching. Therefore, it cannot be exploited for EB techniques simultaneously. For this reason, an implementation with the $h = 18\,480$ system was pursued. The voltage was set to the minimum available voltage of 200 kV (eV $= 50\Delta E$, $\hat{\delta}_b = 1 \times 10^{-4}$), as the measurement tests showed this to be sufficient to obtain acceptable ripple suppression.

A. Extracted intensity

When searching for the optimal rf-frequency offset, one must be aware of certain phenomena that may affect the transparency of the implementation, constraining the allowed values of δ_{rf} in addition to minimizing G. Notably, the obstruction caused by the rf bucket in longitudinal phase space can significantly impact the extracted intensity I_0. For example, if the rf bucket overlaps with the initial beam distribution when the rf is switched on, some beams may be captured. Alternatively, if the rf acceleration is too high, particles may be accelerated too quickly through the resonance, becoming stable again before they can reach the extraction septum.

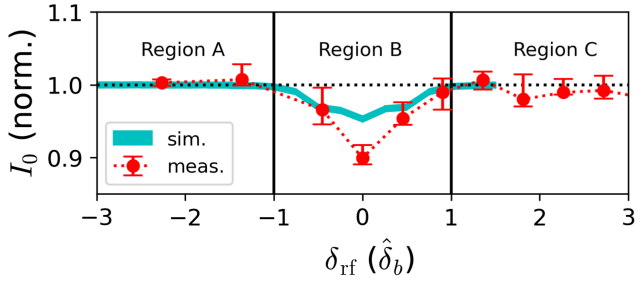

FIG. 15. Total extracted intensity I_0 vs rf offset δ_{rf}, both measured and simulated. Qualitatively, the functional dependence of I_0 can be separated into three regions (A, B, and C) depending on the rf offset with respect to the initial beam distribution.

Figure 15 shows the measured and simulated extracted intensity I_0 as a function of δ_{rf}. The effect of the empty bucket can be categorized into three broad regions: (i) Region A ($\delta_{\mathrm{rf}} \leq -\hat{\delta}_b$): ripple is suppressed due to the large-offset dynamics from Sec. III B. Since the momentum oscillations bring particles in and out of resonance several times, the extracted intensity remains high. (ii) Region B ($-\hat{\delta}_b < \delta_{\mathrm{rf}} < \hat{\delta}_b$): ripple is suppressed due to the small-offset dynamics from Sec. III A. Some particles may be accelerated through the resonant stop band too quickly and become stable again before they gain enough horizontal amplitude to reach the septum. This negatively impacts the extracted intensity and emittance. (iii) Region C ($\delta_{\mathrm{rf}} \geq \hat{\delta}_b$): ripple is suppressed due to the large-offset dynamics from Sec. III B. When switching the rf on, its frequency may coincide with that of the waiting beam, capturing some particles inside the (no longer empty) bucket. This leads to a reduction of extracted intensity, as well as substantial perturbation of the momentum distribution. One could move the beam further away from the resonance, but this would delay the start of the extraction and make the implementation nontransparent to the current mode of operation.

The simulation results qualitatively reproduce the reduction in extracted intensity in region B, verifying that the phenomenon is caused by the acceleration provided by the empty bucket. In order to improve the quantitative agreement, particularly near $\delta_{\mathrm{rf}} = 0$, one should pursue a more complex simulation model with more precise knowledge of the beam and machine parameters. The effect in region C was not simulated, since it is not an intrinsic effect from EB techniques but rather a constraint from the operational implementation. In fact, during the simulation, the initial momentum distribution was offset away from the bucket to avoid beam capture.

It must be noted that in all cases, the nonextracted beam is safely dumped at the end of the flattop and not lost on the aperture, so it could be compensated to a certain extent by injecting more protons per cycle. For the SPS, $\delta_{\mathrm{rf}} = -\hat{\delta}_b$ was selected as an acceptable compromise between ripple suppression and nonextracted (dumped) intensity. An attempt at $\delta_{\mathrm{rf}} = \hat{\delta}_b$ was also made, but it resulted in less reproducible spills due to the proximity of the empty bucket and the waiting stack.

B. Transverse effects

It is important to consider the effect of the longitudinal kicks on the transverse trajectories of resonant particles. Since the manipulation fundamentally relies on chromatic coupling, the longitudinal perturbations caused by the rf will inevitably result in transverse perturbations. These transverse perturbations can alter the presentation of the extracted separatrix on the septum, leading to increased beam loss. In addition to this, the SPS operates with a silicon crystal upstream of the septum, which deflects particles away from the wires and into the extraction channel [26]. If the rf kicks were to significantly affect the transverse distribution of the outgoing separatrix, the efficiency of this technique would also be compromised.

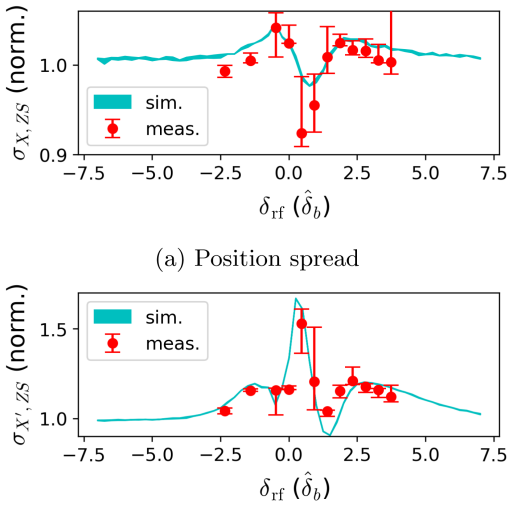

(a) Position spread

(b) Angular spread

FIG. 16. Position and angular spread of the extracted beam at the septum (quantified by the standard deviation). The values have been normalized in the case where the rf is off. The error bars show the shot-to-shot variability.

In order to quantify the effect on the horizontal transverse properties of the extracted beam, we studied the position spread $\sigma_{X,ZS}$ and the angular spread $\sigma_{X',ZS}$ of the extracted beam at the septum. These quantities were measured in the transfer line by choosing two beam-profile monitors with favorable phase advance with respect to the extraction septum. Figure 16 shows the result of such measurement as a function of rf-frequency offset. The simulation predictions are also shown, which are meant to be only indicative due to the vastly simplified lattice model. Still, the functional dependence of both quantities is well modeled, despite their highly nonlinear forms.

For the operational setting ($\delta_{\mathrm{rf}} = -\hat{\delta}_b$), Fig. 17 shows the simulation output in horizontal transverse phase space, as well as the case where the rf is off. It is clear that the case with rf on produces a beam with a wider angular spread. However, this effect was small enough not to compromise the SPS extraction efficiency, resulting in no appreciable increase in beam loss. It is important to note that other configurations did show larger beam loss, making the possible transverse perturbations an important phenomenon to keep in mind when implementing EB techniques in a high-energy high-intensity machine.

C. Longitudinal effects

A final point of consideration concerns longitudinal time structure in the rf-period timescale (1.25 ns in this case).

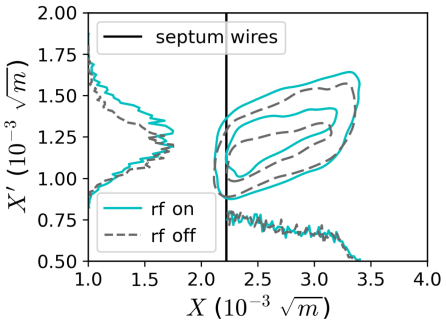

FIG. 17. Simulated horizontal transverse distributions of the extracted beam for the operational implementation (rf on) and the case without rf (rf off). The contours show the 50% and the 95% envelopes.

Inevitably, the time-varying rf kicks will impart some bunching on the outgoing beam. This phenomenon is in principle undesirable for the NA experiments. However, the users reported that the 1.25 ns structure introduced by the $h = 18\,480$ system was acceptable during data taking. First, the timescale is short enough that most experiments lack the resolution to measure it, either due to insufficient particle rate or acquisition speed. Second, the empty bucket is operated at $\delta_{\mathrm{rf}} = -\hat{\delta}_b$ and thus far from perfect alignment between channel and resonance (which would maximize bunching [13]). As demonstrated by the simulation output in Fig. 18, the extracted time profile does show some modulation within an rf period but does not exhibit tight bunching. A comprehensive exploration of employing empty-bucket channeling for delivering bunched beams from the SPS can be found in [24].

D. Long-term experience

Since August 2023, the EB technique has been added as part of nominal fixed target operation in the SPS and has been shown to be fully compatible with the already operational feed-forward compensation that employs all focusing quadrupoles in the ring. Figure 19 shows

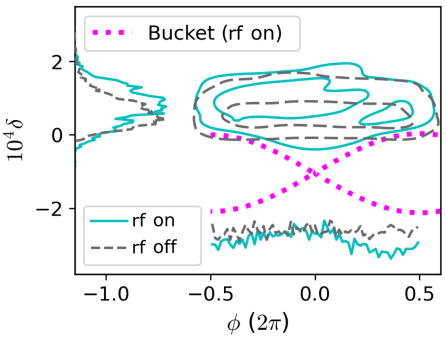

FIG. 18. Simulated longitudinal distribution of the extracted beam (folded into a single rf period) for the operational implementation (rf on) and the case without rf (rf off). The contours show the 50% and the 95% envelopes.

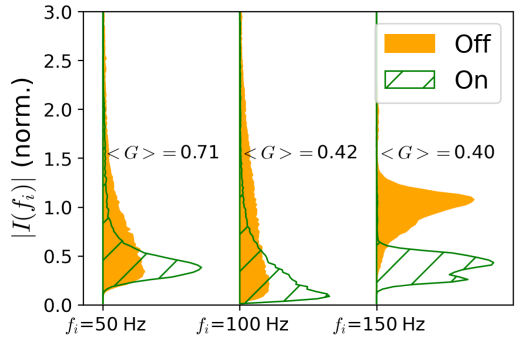

FIG. 19. Spill perturbations $|I(f_i)|$ accumulated over 1 week of SPS operation with rf on and off. The distributions are shown for three relevant ripple frequencies: 50, 100, and 150 Hz. The average ripple-reduction coefficient $\langle G \rangle$ is also shown for each frequency.

histograms of the 50, 100, and 150 Hz spill-ripple magnitudes over a period of 1 week (around 20 k spills) before and after the implementation. The improvement is clear for all three spectral components, both when computing the average suppression factor $\langle G \rangle$ and when visually comparing the distributions directly. The 100 and 150 Hz components show very similar suppression factors, while the 50 Hz suppression factor is smaller. This can be well explained by the fact that smaller f_i has narrower suppression valleys and the values for $\langle G \rangle$ are in fact consistent with those of Fig. 14 when $\delta_{\mathrm{rf}} \approx -\hat{\delta}_b$.

VIII. CONCLUSION

This paper has systematically studied empty-bucket techniques for spill-quality improvement. By combining theory, simulation, and measurement, the dependencies on rf harmonic, rf voltage, rf frequency and ripple frequency have been detailed and the mechanisms for such dependencies explained. While the canonical implementation of EBC (small-offset EB) prescribes the overlap between rf bucket and the resonance stop band, we have shown that this is not a necessary condition for ripple suppression (large-offset EB). Interestingly, the latter configuration does not strictly rely on an accelerating bucket and could therefore be used in any chromatic slow extraction, in a similar fashion to the way conventional bunching is employed.

Additionally, we have described the operational implementation of empty-bucket techniques in the SPS. In this case, external constraints played an important role when selecting the operational parameters. In particular, the rf parameters had to be tuned to avoid an increase in beam loss and/or a reduction in extracted intensity. This was achieved by operating at low rf voltage and by sufficiently offsetting the rf frequency away from the waiting beam.

The tools developed here have already found applicability in the PS. By exploiting a very similar approach, a preliminary implementation of EB techniques has been

tested [27], which could become operational if needed by the East Area experiments. Moreover, a similar modeling paradigm could be exploited to study other ripple-suppression techniques, such as adding longitudinal or transverse noise during the extraction. All in all, this paper demonstrates that rf techniques offer an attractive opportunity to improve spill quality and that they can be successfully modeled by employing computationally efficient approaches.

ACKNOWLEDGMENTS

This work was supported by the Physics Beyond Colliders (PBC) Study Group. The authors thank PBC for their support. The same gratitude is extended to the SPS machine operators and the NA62 experiment for their cooperation during the measurement campaigns.

[1] V. Kain, F. Velotti, M. Fraser, B. Goddard, J. Prieto, L. Stoel, and M. Pari, Resonant slow extraction with constant optics for improved separatrix control at the extraction septum, Phys. Rev. Accel. Beams **22**, 101001 (2019).

[2] B. Dobrich, Highlights and requests from the North Area experiments for proton beams, in *Proceedings of the Injectors and Experimental Facilities Workshop* (CERN, Geneva, 2021).

[3] M. Pari, F. Velotti, M. Fraser, V. Kain, and O. Michels, Characterization of the slow extraction frequency response, Phys. Rev. Accel. Beams **24**, 083501 (2021).

[4] S. Sorge, P. Forck, and R. Singh, Measurements and simulations of the spill quality of slowly extracted beams from the SIS-18 synchrotron, J. Phys. Conf. Ser. **1067**, 052003 (2018).

[5] S. van der Meer, Stochastic extraction, a low-ripple version of resonant extraction, CERN, Technical Report No. CERN-PS-AA-78-6, 1978.

[6] M. Pullia, Dynamique de l'éjection lente et son influence sur les lignes de transfert, Ph.D. thesis, Universite Claude Bernard, Geneva, 1999.

[7] M. Gyr, Low frequency fluctuations of spill rates during slow resonant extraction, CERN, Technical Report No. SPS/89-21, 1989.

[8] R. Singh, P. Forck, and S. Sorge, Reducing fluctuations in slow-extraction beam spill using transit-time-dependent tune modulation, Phys. Rev. Appl. **13**, 044076 (2020).

[9] R. Cappi and C. Steinbach, Low frequency duty factor improvement for the CERN PS slow extraction using RF phase displacement techniques, IEEE Trans. Nucl. Sci. **28**, 2806 (1981).

[10] K. N. Henrichsen and M. J. De Jonge, Acceleration by phase displacement in the ISR, in *Proceedings of the 9th International Conference on the High-Energy Accelerators, Stanford, CA* (A.E.C., Washington, DC, 1975).

[11] A. De Franco, L. Adler, F. Farinon, N. Gambino, G. Guidoboni, G. Kowarik, M. Kronberger, C. Kurfürst, S. Myalski, S. Nowak, L. Penescu, M. Pivi, C. Schmitzer, I. Strašík, P. Urschütz, and A. Wastl, Slow extraction optimization at the MedAustron ion therapy center: Implementation of front end acceleration and RF knock out, in *Proceedings of the 9th International Particle Accelerator Conference, IPAC2018, Vancouver, BC, Canada* (JACoW, Geneva, Switzerland, 2018).

[12] K. Brown, L. Ahrens, J. Brennan, J. Glenn, T. Roser, T. Russo, N. Tsoupas, K. Smith, and K. Zeno, Status of slow extraction of high intensity protons from Brookhaven's AGS, in *Proceedings of the 20th Particle Accelerator Conference, PAC-2003, Portland, OR* (IEEE, New York, 2003), Vol. 3.

[13] S. Koscielniak, High frequency, short bunch width, slow extraction for KOPIO, BNL, Technical Report No. TRI-DN-02-19, 2002.

[14] L. Ahrens, A. Artamonov, G. Atoian, K. Brown, C. Cantley, N. Cartiglia, I. Christidi, J. Glenn, A. Hatzikoutelis, D. Jaffe, S. Koscielniak, D. Lazarus, J. Mabanta, M. Marx, P. Pile, G. Redlinger, C. Scarlett, and M. Sivertz, Interbunch extinction measurement at the BNL AGS for the KOPIO experiment, Nucl. Instrum. Methods Phys. Res., Sect. A **560**, 256 (2006).

[15] M. Pari, Study and development of SPS slow extraction schemes and focusing of secondary particles for the ENUBET monitored neutrino beam, Ph.D. thesis, University of Padua, 2020.

[16] P. A. Arrutia Sota, P. N. Burrows, M. A. Fraser, and F. M. Velotti, Millisecond burst extractions from synchrotrons using rf phase displacement acceleration, Nucl. Instrum. Methods Phys. Res., Sect. A **1039**, 167007 (2022).

[17] P. A. Arrutia Sota, M. A. Fraser, F. M. Velotti, P. N. Burrows, V. Kain, G. Papotti, R. Piandani, F. Roncarolo, A. Spierer, and M. Vadai, RF techniques for spill quality improvement in the SPS, in *Proceedings of the 14th International Particle Accelerator Conference, Venice, Italy* (JACoW, Geneva, Switzerland, 2023).

[18] P. A. Arrutia Sota, G. Hagmann, and G. Papotti, SPS 800 MHz cavity-controllers for empty bucket channelling, CERN, Technical Report No. EDMS 2874819, 2023.

[19] M. Crescenti, RF empty bucket channelling combined with a betatron core to improve slow extraction in medical synchrotrons, CERN, Technical Report No. CERN-PS-97-068-DI, 1998.

[20] S. Y. Lee, *Accelerator Physics*, 4th ed. (World Scientific, Singapore, 2019).

[21] A. De Franco, Summary of RF channelling implementation at MedAustron, EBG MedAustron (private communication).

[22] S. Sorge, P. Forck, and R. Singh, Spill ripple mitigation by bunched beam extraction with high frequency synchrotron motion, Phys. Rev. Accel. Beams **26**, 014402 (2023).

[23] J. Prieto, M. A. Fraser, B. Goddard, V. Kain, L. Stoel, and F. Velotti, Beam dynamics simulations of the effect of power converter ripple on slow extraction at the CERN SPS, in *Proceedings of the 9th International Particle Accelerator Conference, Vancouver, BC, Canada* (JACoW, Geneva, Switzerland, 2018).

[24] P. A. Arrutia Sota, Advanced RF techniques for CERN's future slow-extracted beams, Ph.D. thesis, University of Oxford, 2024.

[25] E. Cortina Gil *et al.*, The beam and detector of the NA62 experiment at CERN, J. Instrum. **12**, P05025 (2017).

[26] F. M. Velotti, L. Esposito, M. A. Fraser, V. Kain, S. Gilardoni, B. Goddard, M. Pari, J. Prieto, R. Rossi, W. Scandale, L. S. Stoel, F. Galluccio, M. Garattini, and Y. Gavrikov, Septum shadowing by means of a bent crystal to reduce slow extraction beam loss, Phys. Rev. Accel. Beams **22**, 093502 (2019).

[27] P. A. Arrutia Sota, P. Burrows, H. Damerau, M. Fraser, M. Vadai, and F. Velotti, Implementation of RF channeling at the CERN PS for spill quality improvements, in *Proceedings of 13th International Particle Accelerator Conference, IPAC-2022, Bangkok, Thailand* (JACoW, Geneva, Switzerland, 2022).